Unravelling the Molecular Structure and Confining Environment of an Organometallic Catalyst Heterogenized within Amorphous Porous Polymers

Ribal Jabbour, Christopher W Ashling, Thomas C Robinson, Arafat Hossain Khan, Dorothea Wisser, Pierrick Berruyer, Ashta C Ghosh, Alisa Ranscht, David A Keen, Eike Brunner, et al.

How to cite: *Angew. Chem. Int. Ed.* **2023**, *62*, e202310878
doi.org/10.1002/anie.202310878

Microporous Materials

Unravelling the Molecular Structure and Confining Environment of an Organometallic Catalyst Heterogenized within Amorphous Porous Polymers**

Ribal Jabbour, Christopher W. Ashling, Thomas C. Robinson, Arafat Hossain Khan, Dorothea Wisser, Pierrick Berruyer, Ashta C. Ghosh, Alisa Ranscht, David A. Keen, Eike Brunner, Jérôme Canivet, Thomas D. Bennett, Caroline Mellot-Draznieks, Anne Lesage,* and Florian M. Wisser**

Abstract: The catalytic activity of multifunctional, microporous materials is directly linked to the spatial arrangement of their structural building blocks. Despite great achievements in the design and incorporation of isolated catalytically active metal complexes within such materials, a detailed understanding of their atomic-level structure and the local environment of the active species remains a fundamental challenge, especially when these latter are hosted in non-crystalline organic polymers. Here, we show that by combining computational chemistry with pair distribution function analysis, ^{129}Xe NMR, and Dynamic Nuclear Polarization enhanced NMR spectroscopy, a very accurate description of the molecular structure and confining surroundings of a catalytically active Rh-based organometallic complex incorporated inside the cavity of amorphous bipyridine-based porous polymers is obtained. Small, but significant, differences in the structural properties of the polymers are highlighted depending on their backbone motifs.

Introduction

Molecular catalysis is a key process for producing goods in our industrialized society and is a powerful tool to improve the sustainability of many processes. The advantages of transferring molecular catalysts from the homogeneous to the heterogeneous phase by immobilization within porous supports are not restricted to site-isolation, easy separation and recycling ability. In fact, the heterogenization of molecular complexes within porous supports has been reported for different reactions, including asymmetric catalysis, photocatalytic water oxidation or CO_2 reduction, to allow for reactivities, productivities and selectivities inaccessible in the homogeneous phase due to the controlled confinement of the active site into a three-dimensional porous framework.[1–8]

The knowledge acquired about the homogeneous molecular catalyst's structure–activity relationship is now so precise that computational chemistry can be used to predict reactivity and selectivity.[9,10] Unfortunately, this level of maturity has not yet been reached for heterogenized molecular catalysts.

[*] Dr. R. Jabbour, T. C. Robinson, Dr. P. Berruyer, Dr. A. Lesage
Centre de RMN à Très Hauts Champs, Université de Lyon (CNRS/ENS Lyon/UCB Lyon 1)
69100 Villeurbanne (France)
E-mail: anne.lesage@ens-lyon.fr
Dr. C. W. Ashling, Prof. Dr. T. D. Bennett
Department of Materials Science and Metallurgy, University of Cambridge
27 Charles Babbage Road, Cambridge CB3 0FS (UK)
Dr. A. H. Khan, Prof. Dr. E. Brunner
Chair of Bioanalytical Chemistry, TU Dresden
Bergstraße 66, 01069 Dresden (Germany)
Dr. D. Wisser, Dr. F. M. Wisser
Erlangen Center for Interface Research and Catalysis (ECRC), Friedrich-Alexander-Universität Erlangen-Nürnberg
Egerlandstraße 3, 91058 Erlangen (Germany)
E-mail: florian.wisser@fau.de
Dr. A. C. Ghosh, A. Ranscht, Dr. J. Canivet
Univ. Lyon, Université Claude Bernard Lyon 1, CNRS, IRCELYON - UMR 5256
2 Avenue Albert Einstein, 69626 Villeurbanne Cedex (France)
Dr. D. A. Keen
ISIS Facility, Rutherford Appleton Laboratory, Harwell Campus
Didcot, Oxfordshire OX11 0QX (UK)
Dr. C. Mellot-Draznieks
Laboratoire de Chimie des Processus Biologiques (LCPB), Collège de France, PSL Research University, CNRS Sorbonne Université
11 Place Marcelin Berthelot,75231 Paris Cedex 05 (France)
E-mail: caroline.mellot-draznieks@college-de-france.fr

[**] A previous version of this manuscript has been deposited on a preprint server (https://doi.org/10.26434/chemrxiv-2022-6d4k9).

Porous organic polymers (POPs) have recently emerged as a new platform to disperse catalytically active complexes.[11–15] Despite these recent achievements in increasing catalytic activity, selectivity or lifetime of the catalyst, little is known about the very local and more distant environment of the metal centre. Notably, the detailed molecular structure of the heterogenized active sites and their confinement-induced interactions with the POP remain unsolved to this date.[16] Even in the case of crystalline metal–organic frameworks (MOFs), which are easier to study than amorphous systems, it is generally assumed that the molecular structure of active sites remains unaltered. However, recent reports have provided evidence that confinement in MOFs (i) affects the structure of heterogenized complexes,[17] (ii) enhances stabilization by Van-der-Waals or π–π-interaction,[7,18] (iii) affects the diastereo- or enantioselectivity in asymmetric catalysis,[7,19] or (iv) alters physicochemical properties.[20] Hence there is a pressing need to develop methodologies to elucidate the precise positioning of functional groups with respect to the pore surface, which is essential for an in-depth understanding of these promising multifunctional materials.[21]

Here we report an integrated methodology combining diffraction and spectroscopic techniques with computational chemistry to unravel the atomic-level structure and confinement of an organometallic rhodium complex embedded within two different POPs. For the first time, detailed and complete pictures of the cavity containing the active sites are provided portraying the catalytic materials, from the first coordination sphere of the metal (≤3.5 Å) to its environment beyond the second coordination sphere (≤7 Å) and the pore structure at the nanometre scale. The structural models obtained by force field simulations are confirmed by a range of experimental evidence, including pair distribution function analysis and dedicated nuclear magnetic resonance (NMR) methodologies that probe short and long-range proximities. The analytical power of the proposed methodology is highlighted by revealing slight but significant differences in the pore structure and the interactions between the metal complex and the polymer walls.

Results and Discussion

Design and Synthesis of the Materials

Recently, we have reported heterogeneous rhodium^{III} pentamethylcyclopentadienyl (Cp*Rh) catalysts within bipyridine containing POPs, namely **Cp*Rh@BpyMP-1** (Figure 1), that showed very promising results in the selective CO_2-to-HCOOH photoreduction and transfer hydrogenation reaction.[22,23] Despite the wide use of the Cp*Rh catalytic unit within porous frameworks,[18,22,31,23–30] its exact molecular structure, positioning and accessibility have remained unexplored due to the particularly challenging structural determination when immobilized in amorphous solids. In particular, the molecular arrangement of the catalyst, including its possible distortion when confined in a micropore and the distances and nature of the interactions between the outer ligand sphere of the catalyst and the pore wall, has never been explored in detail.

In order to get structural insights into the environment of Cp*Rh complexes within POPs, we considered two materials, based on biphenyl motifs functionalized with (^{15}N-labelled) NH_2 or NO_2 groups, providing additional probe nuclei for the NMR studies. The synthesis of the required ^{15}N-labelled monomers was achieved starting from 1,4-dibromo-benzene. In the first step, one NO_2 group was introduced in the 2 position of 1,4-dibromo-benzene (**I**) using ^{15}N-labelled nitric acid (Figure 1, Supporting Informa-

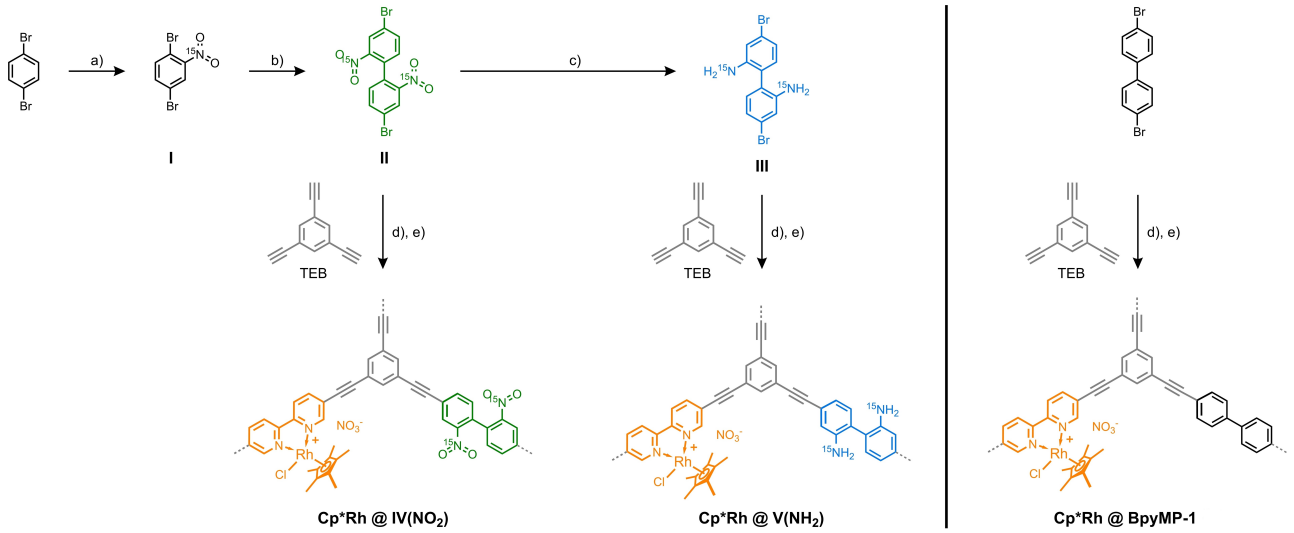

Figure 1. Left: Rection Scheme for the synthesis of **Cp*Rh@IV(NO_2)** and **Cp*Rh@V(NH_2)**, including the synthesis of ^{15}N-labelled monomers 4,4′-dibromo-2,2′-{^{15}N}-dinitro-biphenyl (**II**) and 2,2′-{^{15}N}-diamino-4,4′-dibromo-biphenyl (**III**): a) HNO_3/H_2SO_4 in CH_2Cl_2, 0 °C to RT; b) Cu, DMF 125 °C, 30 min; c) $SnCl_2$, HCl/EtOH, RT 18 h; d) 1 eq. triethynylbenzene (TEB), 0.375 eq. 5,5′-dibromo-2,2′bipyridine, 1.125 eq. **II** or **III**, $Pd(PPh_3)_4$, DMF/NEt_3, 100 °C, 24 h; e) (Cp*RhCl)NO_3, MeOH, 24 h, RT. Right: Reaction scheme for literature-known catalyst **Cp*Rh@BpyMP-1**.[23]

tion section 2). 1,4-dibromo-2-{^{15}N}-nitro-benzene was selectively coupled in the 1 position using the Ullmann cross-coupling reaction to yield 4,4′-dibromo-2,2′-{^{15}N}-dinitro-biphenyl (**II**). In the last step, NO_2 groups were reduced to NH_2 groups using $SnCl_2$ to give 2,2′-{^{15}N}-diamino-4,4′-dibromo-biphenyl (**III**).

Co-polymerization of **II** or **III** with 5,5′-dibromo-2,2′bipyridine and 1,3,5-triethynyl benzene, gave the {^{15}N}-nitro POP **IV(NO$_2$)** or the {^{15}N}-amino POP **V(NH$_2$)**, adapting a literature procedure.[23] Cp*Rh was introduced by infiltration of a methanolic solution of [Cp*RhCl]NO_3 into the materials to provide **Cp*Rh@IV(NO$_2$)** and **Cp*Rh@V-(NH$_2$)**. Using this approach, Rh loadings of approx. 6.0 and 7.0 wt-% for **IV(NO$_2$)** and **V(NH$_2$)** respectively were achieved (Table S2).

The composition and integrity of the different POPs were confirmed by physisorption measurements, IR and solid-state NMR spectroscopies. Nitrogen physisorption at 77 K reveals a microporous character (Figure S1a), with apparent surface areas of ≈330 and ≈480 m^2/g for **Cp*Rh@IV(NO$_2$)** and **Cp*Rh@V(NH$_2$)**, respectively, in line with reported values for similar materials (280–610 m^2/g, see Supporting Information section 4).[23] Both materials also show significant CO_2 uptake at 273 K (Figure S1b). In the IR spectra, no signal around 2100 cm^{-1} (ν_{as}C≡CH), characteristic of unreacted terminal ethynyl moieties,[32] can be detected (Figure S3), indicative for a high degree of polymerization.[32,33] The presence of the NO_2 groups in **IV(NO$_2$)** is evidenced by its characteristic vibrations at 1530 and 1350 cm^{-1}, while the presence of NH_2 groups in **V(NH$_2$)** is evidenced by the N–H stretching vibrations between 3470 and 3190 cm^{-1} (Figure S3).

Molecular Composition from DNP SENS

Over the last decade, Dynamic Nuclear Polarization Surface-Enhanced NMR spectroscopy (DNP SENS) has emerged as a powerful approach for an in-depth structural characterization of functionalized surfaces and materials.[34,35] Following the first proofs of concepts reported on mesoporous silicas,[36,37] recent applications have successfully covered a much wider range of materials.[38–42] In particular, we and others have demonstrated the relevance of this methodology for the investigation of the backbone structure of POPs.[23,43–45]

One- and two-dimensional DNP SENS spectra were recorded to address the molecular composition of **Cp*Rh@IV(NO$_2$)** and **Cp*Rh@V(NH$_2$)**. NMR data were also recorded on the non-functionalized **Cp*Rh@BpyMP-1**. As described in the experimental section, the materials were impregnated by incipient wetness with solutions of TEKPOL in 1,1,2,2-tetrachloroethane (TCE) and signal enhancements of around 20 were obtained for the polymer's ^{13}C resonances at 9.4 T (Figure S4), while as expected, more moderate enhancement factors (of around 3) were measured at 18.8 T.

The DNP-enhanced ^{13}C CPMAS (Cross Polarization Magic Angle Spinning) spectra exhibit the expected aromatic resonances in the 120–150 ppm range, as well as the C≡C signal at 90 ppm of the polymer backbone (Figure 2Figure 2a and Figure S5). The additional resonance at

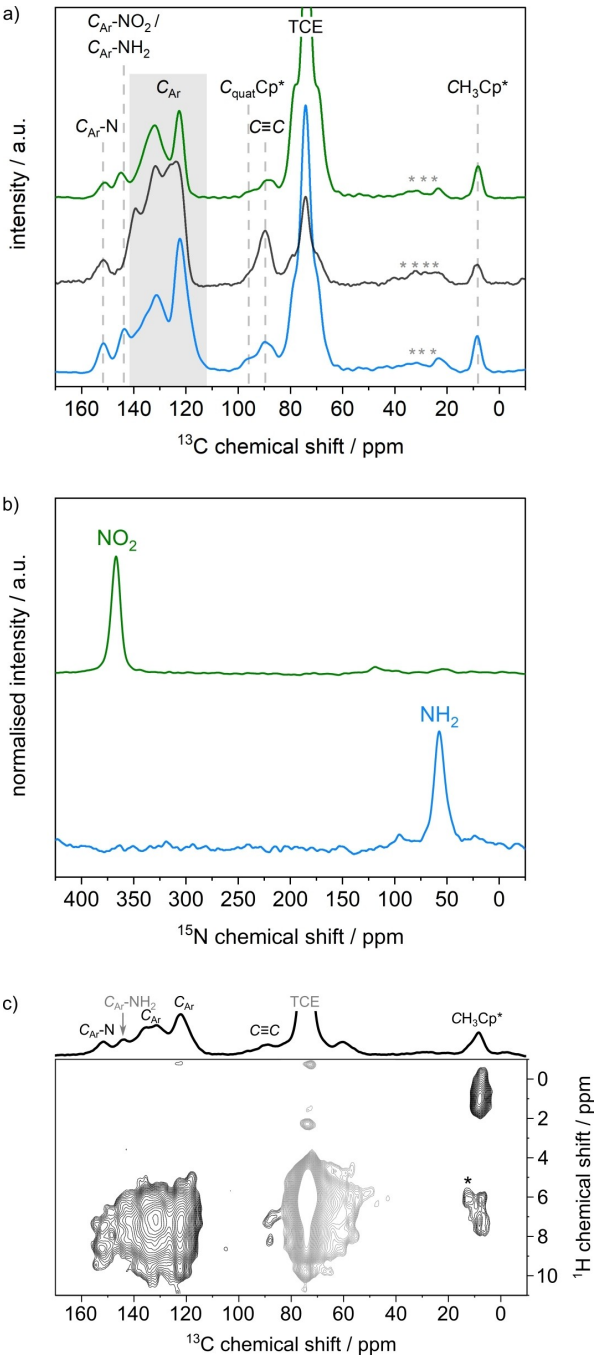

Figure 2. a) DNP SENS ^{13}C CPMAS spectra of **Cp*Rh@V(NH$_2$)** (blue), **Cp*Rh@BpyMP-1** (black) and **Cp*Rh@V(NO$_2$)** (green) recorded at 9.4 T and 10 kHz MAS. Asterisks denote spinning sidebands. b) DNP SENS ^{15}N CPMAS spectra of **Cp*Rh@V(NH$_2$)** (blue) and **Cp*Rh@IV-(NO$_2$)** (green) recorded at 9.4 T and 10 kHz MAS. c) DNP SENS ^{1}H-^{13}C HETCOR spectrum of **Cp*Rh@V(NH$_2$)** along with the corresponding 1D carbon-13 spectrum recorded at 18.8 T and 12.5 kHz MAS. The strong correlation at about 72 ppm in the carbon and 6 ppm in the proton dimensions is due to TCE signal, its spinning sideband (*) does not overlap with other correlations.

≈143 ppm in the spectra of **Cp*Rh@IV(NO_2)** and **Cp*Rh@IV(NH_2)**, can be readily assigned to the carbon atom bonded to the functional NO_2 or NH_2 group (Figure 2a). The resonances at 96.6 and 8.5 ppm correspond to the quaternary carbons and methyl groups of the Cp* moiety, respectively.

The DNP-enhanced nitrogen-15 CPMAS spectra further confirm the integration of either NO_2 (366 ppm) or NH_2 groups (57 ppm) into **Cp*Rh@IV(NO_2)** and **Cp*Rh@V(NH_2)**, respectively. The agreement of the ^{15}N chemical shift between monomers and polymers as well as the absence of any further peak excludes any chemical modification or metal coordination of the NO_2/NH_2 groups (Figure 2b and Figure S6).

The molecular composition of the materials was further confirmed using ^{1}H–^{13}C dipolar-based heteronuclear correlation (HETCOR) experiments. These data were acquired at a higher magnetic field to improve resolution in the indirect (proton) dimension. The ^{1}H–^{13}C HETCOR spectrum of **Cp*Rh@V(NH_2)** (Figure 2c) shows strong correlations between aromatic protons centred at 7 ppm and the carbon resonances at 151.6, 143.6, 135.5, 131.3, and 122.0 ppm. In addition, a cross-peak is observed between the methyl carbon and proton resonances centred at 8.5 ppm and 1 ppm, respectively. The correlation signal between aromatic protons at 6–7 ppm and the methyl carbon atoms at 8.5 ppm indicates close proximity between the Cp* ligand and the surrounding pore wall in **Cp*Rh@V(NH_2)**. A similar correlation was observed for **Cp*Rh@BpyMP-1** (Figure S7). The absence of any correlation around 80 ppm in the carbon dimension, characteristic ^{13}C chemical shift of unreacted terminal ethynyl moieties,[32] and ca. 3 ppm in the proton dimension, characteristic proton chemical shift of unreacted terminal ethynyl moieties,[46] demonstrates that hardly any unreacted end-groups remain in the materials.

Polymer Linkage by Quantitative ^{13}C MAS NMR

To obtain detailed insight into the number of unreacted end-groups, quantitative (q) ^{13}C MAS spectra were recorded. Deconvolution of the q-^{13}C signals observed between 80 and 90 ppm reveals less than 5 % of unreacted end-groups remaining in the polymers (Figures S10, S11).[33,47] From the number of unreacted end-groups the probability that 1,3,5-triethynylbenzene (TEB) moieties have reacted once, twice or three times was calculated. Here, we applied the ideal network assumption for cross-linked polymers, i.e. assuming (i) the same reactivity of bipyridine- and biphenyl-based B2-type monomers, (ii) that all groups react independently from each other, and (iii) a stepwise copolymerisation between A3-type monomer (TEB) and B2-type monomers.[48,49] The probability of TEB moieties to be a cross-linkage ($m=3$), a linear linkage ($m=2$) or to be a dangling end-group could thus be calculated using the following equation:

$$P(X_m) = \binom{3}{m} \cdot \left(\frac{1 - r \cdot p^2}{r \cdot p^2}\right)^{3-m} \cdot \left[1 - \left(\frac{1 - r \cdot p^2}{r \cdot p^2}\right)^{m}\right] \quad (1)$$

with r the stoichiometric ratio of functional groups ($r \leq 1$), p the conversion of ethynyl groups obtained from q-^{13}C NMR and m the number of ethynyl groups reacted per TEB molecule. Whatever the functionalisation of the linear monomer used, we found that ≈76 % of the TEB moieties are fully branched, ≈22 % are linearly linked and only 2 % are dangling end-groups (Table S2). Those results were confirmed by ^{1}H spectra yielding a branching probability of approx. 80 % (SI section 5.3). This result highlights that important insights about the structure and composition of POPs can be obtained from ^{1}H MAS NMR spectroscopy.

Structural Models of Porous Polymers

Based on the required information on the polymers' composition from NMR we have undertaken a computational approach to build plausible structural models of **Cp*Rh@IV(NO_2)** and **Cp*Rh@V(NH_2)** frameworks. In a first step, DFT-D3 level geometry optimizations of each repeating molecular unit, i.e. TEB-biphenyl(NH_2)$_2$-TEB, TEB-biphenyl(NO_2)$_2$-TEB and TEB-Cp*Rh@bpy-TEB, were performed prior the construction of each polymer model (see Supporting Information section 7 for details). In a second step, models of both polymers were grown in a stepwise fashion using the DFT geometry-optimized repeating units and attaching covalently either a biphenyl(NH_2)$_2$-TEB or a biphenyl(NO_2)$_2$-TEB unit to a [Cp*Rh@bpy]-TEB repeating unit through its terminal ethynyl groups. The **Cp*Rh@IV(NO_2)** and **Cp*Rh@V(NH_2)** polymers were thus both grown sequentially using the experimental Cp*Rh@bpy : biphenyl ratio as a guideline. Considering the very large size reached for both resulting structural models (≈25 units lead to simulation boxes of more than 80 Å edge), geometry optimizations of both polymers were performed at each construction step using the generic universal forcefield (see Supporting Information section 7).[50]

Interestingly, the construction and optimization steps resulted in entangled structures (Figure 3). The entanglement allows recurrent π-π interactions between biphenyl and TEB moieties within distances of 3.6–4.1 Å (Table S4). Notably, the TEB–Cp*Rh@bpy-TEB units were found in both models close to branching TEB moieties, placing the Cp*Rh-complex in the vicinity of NH_2 or NO_2 groups of neighbouring biphenyls, with $C_{(CH3)}\cdots N_{(NH2/NO2)}$ distances in the 3.8–7.0 Å range (Table S4). In the **Cp*Rh@IV(NO_2)** structural model, the entanglement of the polymer allows the occurrence of π–π interactions between Cp*Rh and a neighbouring biphenyl linker (Figure S16), bringing several methyl groups of the Cp* moiety close to one NO_2 group (Figure 3c), with interatomic $C_{(CH3)}\cdots N$ distances of 3.8–6.4 Å. The next closest pore wall is at a $C_{(CH3)}\cdots N_{(NO2)}$ distance of 10–12 Å. We do not observe such π-π interactions in **Cp*Rh@V(NH_2)**, which might be due to less

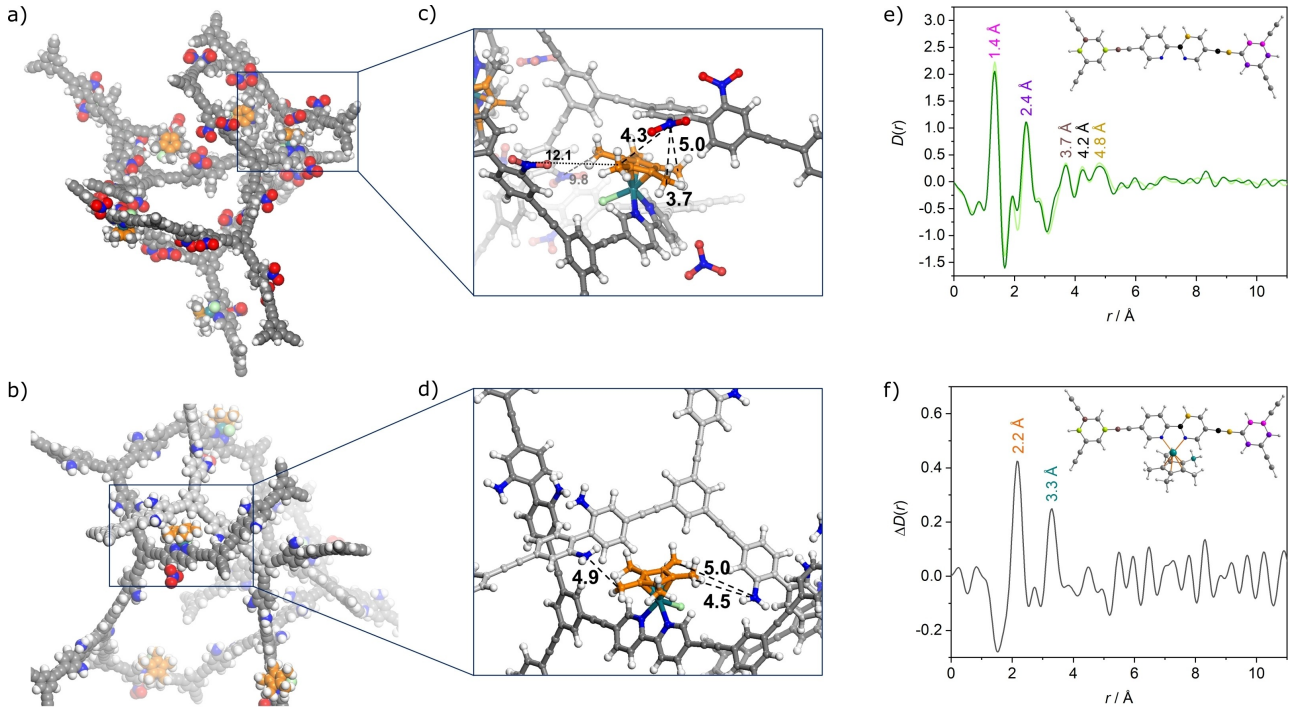

Figure 3. a) and b) Computed structural models for **Cp*Rh@IV(NO_2)** and **Cp*Rh@V(NH_2)**, respectively. c) and d) Local environment of a Cp*Rh moiety in **Cp*Rh@IV(NO_2)** and **Cp*Rh@V(NH_2)**, respectively, highlighting selected $C_{(CH3)}$···$N_{(NO2)}$ and $C_{(CH3)}$···$N_{(NH2)}$ intermolecular distances between the CH_3 of Cp* (in orange) and NO_2 or NH_2 groups of the polymer backbone. Colour code: C in grey, H in white, N in blue, O in red and Rh in turquoise. e) PDF of **IV(NO_2)** (light green) and **Cp*Rh@IV(NO_2)** (green), f) corresponding d-PDF together with DFT optimized molecular clusters. Coloured atoms in the molecular structures in PDF / d-PDF illustrate the interatomic distances detected by PDF analysis and follow the same colour code (other possible pairs of atoms for $d \geq 3.7$ Å are shown in Figure S14b). The interatomic C–C distance across one benzene ring (light green) is hardly visible.[52] In the d-PDF (f), the distances of rhodium's primary coordination sphere are indicated by orange lines (Rh···N, and Rh···C), of its secondary coordination sphere are illustrated by one pair of atoms in cyan (Rh and one CH_3-carbon). Cl^- and NO_3^- are omitted for clarity.

beneficial electronic interaction between electron-rich Cp* and electron-rich biphenyl(NH_2)$_2$-moieties compared to the Cp* interaction with electron-poor biphenyl(NO_2)$_2$-moieties in **Cp*Rh@IV(NO)$_2$**. Similarly, π-π interactions have been reported between Cp* ligands and electron-deficient linkers in MOFs.[18]

Another situation is illustrated in Figure 3d in the **Cp*Rh@V(NH_2)** model, where the methyl carbon atoms of the Cp* moiety are embedded between two NH_2 groups belonging to two different biphenyl(NH_2)$_2$ ligands of a branching TEB node, resulting in slightly longer interatomic $C_{(CH3)}$···N distances of 4.4–6.0 Å as compared to **Cp*Rh@IV-(NO_2)**.

To validate these plausible structural models and to confirm experimentally the discussed changes in long-range distances (vicinity of RhCp* to NH_2/NO_2 groups) between the two polymers, pair distribution function analysis as well as advanced ^{129}Xe and Rotational Echo-Double Resonance NMR experiments were performed (see below).

First Coordination Sphere from PDF Analysis

To explore experimentally the coordination sphere of the Rh atom in the heterogenized molecular complex, total scattering experiments were performed. The pair distribution functions (PDFs) of **IV(NO_2)** and **Cp*Rh@IV(NO_2)** were gained by Fourier transforming the structure factors $S(Q)$ (Figure S13a). The PDFs, $D(r)$ show local structural information such as inter-atomic distances between pairs of atoms even from amorphous materials.[51] Both PDFs display features up to 5 Å, though they are relatively featureless after this point (Figure 3e and Figure S13b), consistent with the amorphous nature of the materials. Peaks at 1.4, 2.4, 3.7, 4.2 and 4.8 Å are attributed to interatomic carbon-carbon distances across one to four C–C bonds of the backbone (Figure 3e, f).[52]

Those correlations overlap with those arising from the heterogenized Cp*Rh-complex. To visualize the contributions from Cp*Rh, we applied a differential PDF (d-PDF) approach.[53] While the application of PDF and d-PDF has been extended to study amongst other local ordering in MOFs,[51,54,55] or the molecular structure of adsorbed species in MOFs and COFs,[56–60] to the best of our knowledge no study concerning the molecular structure of an organometallic complex within an amorphous polymer has been reported yet.

The d-PDF highlights two additional interatomic distances below 5 Å for **Cp*Rh@IV(NO_2)** (Figure 3f). The distance peak centred at 2.2 Å corresponds to the intra-

molecular distances of both the Rh–N and the Rh–$C_{(quart\ Cp^*)}$ bonds. The distance peak at 3.3 Å is assigned to the intramolecular distances between the Rh centre and the $C_{(CH3)}$ of the Cp* moiety. Those distances fit perfectly with the distances that are obtained from single crystal analysis of Cp*Rh(bpe-bpy)Cl_2, proving that no significant distortion of the molecular geometry is caused by the confinement. Furthermore, they are in line with the distances obtained from the plausible structural models (Table S3), providing the first evidence that these models reflect the structure in the amorphous polymers.

Pore Size by ^{129}Xe Adsorption Experiments at 237 K

To estimate the average pore size in these materials, we implemented ^{129}Xe NMR spectroscopy. Since the seminal paper from Ito and Fraissard,[61] ^{129}Xe NMR has become an important tool to probe the average pore size of modern materials.[62,63]

In the ^{129}Xe NMR spectra measured at 237 K and at a relative pressure of 1, the signal at approx. 197 ppm can be attributed to bulk liquid xenon (Figure 4a). The low field shifted signal present in all spectra is attributed to xenon interacting with the pore walls of the different materials, its chemical shift increases with decreasing pore diameter.[64,65] To correlate the chemical shift of absorbed xenon with the pore size, a series of Zr-based MOFs with known pore size was used as reference materials (see Supporting Information section 5.4). Average pore sizes of 10.0 Å (**Cp*Rh@IV-(NO_2)**) and 10.5 Å (**Cp*Rh@V(NH_2)**) are obtained (Figure 4b). A possible explanation for the smaller pore size of **Cp*Rh@IV(NO_2)** might be weaker interactions between the growing polymer chain and the solvent used during synthesis. While NO_2 groups can act as H-bond acceptors (from triethylamine), NH_2 groups in **V(NH_2)** can act as H-bond acceptors and donors. The weaker interaction during the synthesis of **IV(NO_2)** may thus result in a more pronounced macrophase separation as observed for other nitro-functionalised POPs.[66]

Thus, the ^{129}Xe NMR data experimentally verify (i) the pore wall distance ($C_{(CH3)}$···$N_{(NO2/NH2)}$ distance) of 10–12 Å and (ii) the tendency of shorter average distances between the backbone of the polymer and the Rh complex in **Cp*Rh@IV(NO_2)** observed in the computational models.

Confinement Beyond the Second Coordination Sphere by $^{13}C\{^{15}N\}$ REDOR DNP SENS Experiments

In the past, Rotational Echo-Double Resonance (REDOR) has been used to study e.g. spatial distribution of functional groups,[67] distances in molecular vices,[68] or defect alignment in crystalline MOFs with mixed linkers.[69] In parallel, the sensitivity boost provided by DNP has recently enabled the measurement of long-range proximities between supported metal complexes and solid surfaces via the implementation of REDOR experiments over long evolution times.[70,71] To further corroborate the structural features revealed by atomistic simulations, $^{13}C\{^{15}N\}$ REDOR DNP SENS experiments were carried out on **Cp*Rh@V(NO_2)** and **Cp*Rh@V-(NH_2)**. In these experiments, ^{13}C–^{15}N heteronuclear dipolar couplings that are averaged out by MAS are reintroduced by applying rotor-synchronized π pulses to nitrogen-15 nuclei, during a dipolar recoupling period which is progressively incremented. Two sets of experiments are recorded for each recoupling time, one where the nitrogen pulses were omitted to get a reference spectrum (of signal intensity S_0) and a second (of signal intensity S), where the dipolar interaction is reintroduced. Figure 4c shows the intensity ratio S/S_0 as a function of the recoupling times for the carbon-13 resonance of the methyl groups at 8.5 ppm. Dephasing curves corresponding to aromatic resonances are provided in Figure S8. The REDOR curves were analysed considering that both polymers were fully ^{15}N-enriched on the NH_2 and NO_2 groups. As the N atoms of the bipyridine motifs bearing the metal centre are not ^{15}N-labelled and therefore only present in 0.37 % natural abundance, the dephasing of the CH_3 signal arises from spatial proximities with NO_2/NH_2 groups. The slope of the dephasing curve

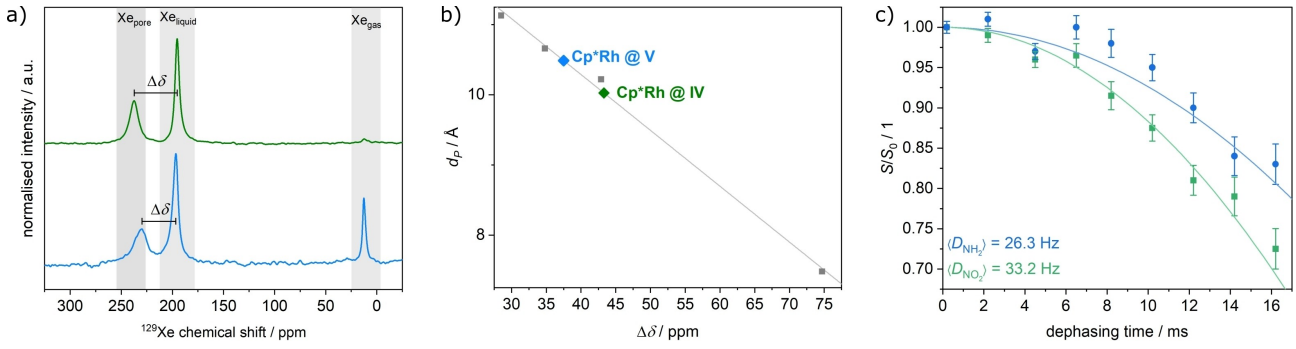

Figure 4. a) ^{129}Xe NMR spectra recorded at 237 K and $p/p_0 = 1$ for **Cp*Rh@IV(NO_2)** (green) and **Cp*Rh@V(NH_2)** (blue). b) ^{129}Xe NMR calibration curve (grey) of pore sizes as a function of measured $\Delta\delta$, determined on different Zr-based MOFs with known pore sizes, together with the pore sizes for **Cp*Rh@IV(NO_2)** (green) and **Cp*Rh@V(NH_2)** (blue). Details are provided in Section S 5.4. c) Experimental $^{13}C\{^{15}N\}$ REDOR dephasing curve up to 16 ms measured for **Cp*Rh@IV(NO_2)** (green dots) and **Cp*Rh@V(NH_2)** (blue dots). The solid lines are the theoretical dephasing curve for an average dipolar coupling value extracted from the structural models.

reflects the size of the dipole – dipole interactions and can in principle be interpreted in terms of ^{13}C–^{15}N internuclear distances in a system of isolated dipolar-coupled spin pairs and then compared to the experimentally measured S/S_0 values.[72] However, the analysis may be complicated by multiple heteronuclear dipolar coupling interactions[73,74] as well as by a distribution of ^{15}N–^{13}C distances.

In the limit of short dipolar evolution times ($S/S_0 < 0.2$–0.3), Bertmer and Eckert showed that for multi-spin interactions (here a ^{13}C spin coupled to multiple ^{15}N spins),[74] a geometry-independent assessment of the dipolar coupling strength can be obtained using a first-order approximation according to the following equation:

$$\frac{S}{S_0} = 1 - \frac{16}{15} \cdot \tau^2 \cdot \left(\sum_{i=1}^{n} D_i^2 \right) \quad (2)$$

where τ is the dephasing time and D_i the dipolar coupling constants of different ^{13}C–^{15}N spin pairs with

$$D_i = \frac{\gamma_I \cdot \gamma_S \cdot \hbar}{2 \cdot \pi \cdot r_i^3} \cdot \frac{\mu_0}{4 \cdot \pi} \quad (3)$$

The experimental curves were fitted up to 16 ms, yielding $\sum D_i^2$ of 1060 ± 50 and 600 ± 70 Hz^2 for **Cp*Rh@IV-(NO_2)** and **Cp*Rh@IV(NH_2)**, respectively (Figure S9). The higher $\sum D_i^2$ is indicative of larger dipolar couplings (for the same number of terms) or of more terms in the sum (due to multiple couplings). This in turn suggests that the pore size is smaller in **Cp*Rh@IV(NO_2)**.

In an alternative way to interpret the REDOR data, we used the ^{15}N–^{13}C distances up to 7 Å from the computed structural models (Table S4) to extract average dipolar coupling constants. Subsequently, the theoretical REDOR curves were calculated, using the exact analytical function (see Supporting Information section 5.1). Remarkable agreements with the experimental data are observed for those long-range distances (Figure 4c), providing the strongest evidence for the soundness of the calculated models. Thus, the REDOR data further support the finding that the pores slightly contract when NH_2 are substituted by NO_2 groups.

Based on the calculated model we concluded that most of the $C_{(CH3)}\cdots N_{(NH2/NO2)}$ distances are in a range of 3.8 to 6.4 Å for **Cp*Rh@V(NO_2)** and in a range of 4.4 to 6.0 Å for **Cp*Rh@V(NH_2)**. Moreover, as the uptake of the solvents TCE (used in DNP) and acetonitrile (used in photocatalysis) are comparable at similar pressure (Figure S2), the results from REDOR, and thus from computational chemistry, can be translated to the photocatalytic conditions in the CO_2-to-HCOOH model reaction (Figure S17). The similar $C_{(CH3)}\cdots N_{(NH2/NO2)}$ distances, as well as pore openings of $\approx$10 Å, confirm experimentally that the accessibility of the active Cp*Rh-site for the $[Ru(bpy)_3]^{2+}$ photosensitizer is not restricted, which in turns is seen in the similar catalytic activity of ≈ 3 mmol$_{CO2}$/h/g$_{cat}$ (Figure S17).

Conclusion

In summary, we characterized the molecular structure and local environment of an organometallic complex heterogenized within amorphous POPs with an unprecedented level of detail. We propose accurate molecular pictures established by computational chemistry approaches that could only be confirmed by a range of advanced DNP surface-enhanced NMR techniques as well as ^{129}Xe NMR and PDF analysis. Importantly, the molecular structure of the heterogenized organometallic moiety is not altered by the confinement within POPs, the intramolecular distances in the first coordination sphere of the central Rh atom being the same as in molecular model clusters. Additionally, our results show that the overall ligand-pore wall distances, as well as the pore size, are affected by the functionalisation of the polymer, yielding significantly stronger $C_{(CH3)}\cdots N$ dipolar couplings for the POP with NO_2 groups, compared to the one with smaller NH_2 groups. Using ^{129}Xe NMR spectroscopy, pore diameters of 10.0 Å (**Cp*Rh@IV(NO_2)**) and 10.5 Å (**Cp*Rh@V(NH_2)**) were obtained, providing experimental evidence for the size of substrates which can access the Rh catalytically active site within a porous matrix. This information corroborates literature reports on the catalytic activity of Cp*Rh functionalised POPs, which suggested no diffusion limitation for small substrates (cross-section $\approx 5\times7$ Å^2) to occur.[22–24] Precise knowledge of the molecular structure of an organometallic complex heterogenized within a porous support material and of its interactions with the surrounding pore is expected to open new perspectives for the design of novel discrete molecular catalysts heterogenized within chemically stable microporous polymers.

Acknowledgements

Financial support of this work by the Deutsche Forschungsgemeinschaft (DFG, German Research Foundation) project-ID WI 4721/1-1 & WI 4721/3-1(F.M.W) and within SPP 2248 and FOR 2433 (E.B.), by the CNRS (Momentum 2018 excellence grant, F.M.W.), by the Royal Society (RG160498, C.W.A.), by the Commonwealth Scientific and Industrial Research Council (C2017/3108, C.W.A.), by the IR INFRANALYTICS FR2054 (F.M.W., A.L.) and by the European Union's Horizon 2020 research and innovation program (no. 101008500, "PANACEA") are gratefully acknowledged. The calculations were performed using the HPC resources from GENCI (CINES/TGCC/IDRIS) through the grant A013097343 (C.M.D.). The authors are grateful to Dr. E. Jeanneau for single crystal measurements, to C. Lorentz for ComPmultiCP MAS NMR, to P. Mascunan for ICP-OES analysis, to Prof. Dr. G. Kickelbick for CHN-analysis, and to Dr. O. Ouari and Prof. Dr. P. Tordo for providing TEKPOL. Open Access funding enabled and organized by Projekt DEAL.

Conflict of Interest

The authors declare no conflict of interest.

Data Availability Statement

The data that support the findings of this study are available from the corresponding author upon reasonable request.

Keywords: Dynamic Nuclear Polarization · Molecular Structure · Nuclear Magnetic Resonance Spectroscopy · Pair Distribution Function · Porous Organic Polymers

[1] J. M. Thomas, R. Raja, *Acc. Chem. Res.* **2008**, *41*, 708–720.
[2] X. Liu, S. Inagaki, J. Gong, *Angew. Chem. Int. Ed.* **2016**, *55*, 14924–14950.
[3] Z. Chen, E. Vorobyeva, S. Mitchell, E. Fako, M. A. Ortuño, N. López, S. M. Collins, P. A. Midgley, S. Richard, G. Vilé, J. Pérez-Ramírez, *Nat. Nanotechnol.* **2018**, *13*, 702–707.
[4] A. Wang, J. Li, T. Zhang, *Nat. Chem. Rev.* **2018**, *2*, 65–81.
[5] Z. Ren, Y. Liu, Y. Lyu, X. Song, C. Zheng, S. Feng, Z. Jiang, Y. Ding, *J. Catal.* **2019**, *369*, 249–256.
[6] T.-Y. Zhou, B. Auer, S. J. Lee, S. G. Telfer, *J. Am. Chem. Soc.* **2019**, *141*, 1577–1582.
[7] J. Canivet, E. Bernoud, J. Bonnefoy, A. Legrand, T. K. Todorova, E. A. Quadrelli, C. Mellot-Draznieks, *Chem. Sci.* **2020**, *11*, 8800–8808.
[8] Y. Quan, Y. Song, W. Shi, Z. Xu, J. S. Chen, X. Jiang, C. Wang, W. Lin, *J. Am. Chem. Soc.* **2020**, *142*, 8602–8607.
[9] J. P. Reid, M. S. Sigman, *Nat. Chem. Rev.* **2018**, *2*, 290–305.
[10] A. R. Rosales, J. Wahlers, E. Limé, R. E. Meadows, K. W. Leslie, R. Savin, F. Bell, E. Hansen, P. Helquist, R. H. Munday, O. Wiest, P.-O. Norrby, *Nat. Catal.* **2019**, *2*, 41–45.
[11] N. Chaoui, M. Trunk, R. Dawson, J. Schmidt, A. Thomas, *Chem. Soc. Rev.* **2017**, *46*, 3302–3321.
[12] J. Chakraborty, I. Nath, S. Song, S. Mohamed, A. Khan, P. M. Heynderickx, F. Verpoort, *J. Photochem. Photobiol. C* **2019**, *41*, 100319.
[13] J.-S. M. Lee, A. I. Cooper, *Chem. Rev.* **2020**, *120*, 2171–2214.
[14] Y. Tian, G. Zhu, *Chem. Rev.* **2020**, *120*, 8934–8986.
[15] F. M. Wisser, Y. Mohr, E. A. Quadrelli, J. Canivet, *ChemCatChem* **2020**, *12*, 1270–1275.
[16] D. Taylor, S. J. Dalgarno, Z. Xu, F. Vilela, *Chem. Soc. Rev.* **2020**, *49*, 3981–4042.
[17] J. Liu, T. A. Goetjen, Q. Wang, J. G. Knapp, M. C. Wasson, Y. Yang, Z. H. Syed, M. Delferro, J. M. Notestein, O. K. Farha, J. T. Hupp, *Chem. Soc. Rev.* **2022**, *51*, 1045–1097.
[18] X. Wang, F. M. Wisser, J. Canivet, M. Fontecave, C. Mellot-Draznieks, *ChemSusChem* **2018**, *11*, 3315–3322.
[19] C. Kutzscher, G. Nickerl, I. Senkovska, V. Bon, S. Kaskel, *Chem. Mater.* **2016**, *28*, 2573–2580.
[20] B. Coasne, D. Farrusseng, *Microporous Mesoporous Mater.* **2019**, *288*, 109561.
[21] Z. Li, T. He, Y. Gong, D. Jiang, *Acc. Chem. Res.* **2020**, *53*, 1672–1685.
[22] F. M. Wisser, Y. Mohr, E. A. Quadrelli, D. Farrusseng, J. Canivet, *ChemCatChem* **2018**, *10*, 1778–1782.
[23] F. M. Wisser, P. Berruyer, L. Cardenas, Y. Mohr, E. A. Quadrelli, A. Lesage, D. Farrusseng, J. Canivet, *ACS Catal.* **2018**, *8*, 1653–1661.
[24] F. M. Wisser, M. Duguet, Q. Perrinet, A. C. Ghosh, M. Alves-Favaro, Y. Mohr, C. Lorentz, E. A. Quadrelli, R. Palkovits, D. Farrusseng, C. Mellot-Draznieks, V. Waele, J. Canivet, *Angew. Chem. Int. Ed.* **2020**, *59*, 5116–5122.
[25] M. B. Chambers, X. Wang, N. Elgrishi, C. H. Hendon, A. Walsh, J. Bonnefoy, J. Canivet, E. A. Quadrelli, D. Farrusseng, C. Mellot-Draznieks, M. Fontecave, *ChemSusChem* **2015**, *8*, 603–608.
[26] F. Gao, R. Jin, D. Zhang, Q. Liang, Q. Ye, G. Liu, *Green Chem.* **2013**, *15*, 2208–2214.
[27] H. Zhang, R. Jin, H. Yao, S. Tang, J. Zhuang, G. Liu, H. Li, *Chem. Commun.* **2012**, *48*, 7874–7876.
[28] Y. Deng, M. Odziomek, C. Sanchez, O. Back, V. Mougel, M. Fontecave, *ChemCatChem* **2020**, *12*, 1236–1243.
[29] Y. Tian, Y. Zhou, Y. Zong, J. Li, N. Yang, M. Zhang, Z. Guo, H. Song, *ACS Appl. Mater. Interfaces* **2020**, *12*, 34795–34805.
[30] Z. Zhao, D. Zheng, M. Guo, J. Yu, S. Zhang, Z. Zhang, Y. Chen, *Angew. Chem. Int. Ed.* **2022**, *61*, e202200261.
[31] J. Everaert, K. Leus, H. Rijckaert, M. Debruyne, K. Van Hecke, R. Morent, N. De Geyter, V. Van Speybroeck, P. Van Der Voort, C. V. Stevens, *Green Chem.* **2023**, *25*, 3267–3277.
[32] M. Trunk, A. Herrmann, H. Bildirir, A. Yassin, J. Schmidt, A. Thomas, *Chem. Eur. J.* **2016**, *22*, 7179–7183.
[33] A. Laybourn, R. Dawson, R. Clowes, T. Hasell, A. I. Cooper, Y. Z. Khimyak, D. J. Adams, *Polym. Chem.* **2014**, *5*, 6325–6333.
[34] A. J. Rossini, A. Zagdoun, M. Lelli, A. Lesage, C. Copéret, L. Emsley, *Acc. Chem. Res.* **2013**, *46*, 1942–1951.
[35] A. S. Lilly Thankamony, J. J. Wittmann, M. Kaushik, B. Corzilius, *Prog. Nucl. Magn. Reson. Spectrosc.* **2017**, *102–103*, 120–195.
[36] A. Lesage, M. Lelli, D. Gajan, M. A. Caporini, V. Vitzthum, P. Miéville, J. Alauzun, A. Roussey, C. Thieuleux, A. Mehdi, G. Bodenhausen, C. Coperet, L. Emsley, *J. Am. Chem. Soc.* **2010**, *132*, 15459–15461.
[37] M. Lelli, D. Gajan, A. Lesage, M. A. Caporini, V. Vitzthum, P. Miéville, F. Héroguel, F. Rascón, A. Roussey, C. Thieuleux, M. Boualleg, L. Veyre, G. Bodenhausen, C. Coperet, L. Emsley, *J. Am. Chem. Soc.* **2011**, *133*, 2104–2107.
[38] P. Berruyer, L. Emsley, A. Lesage, *eMagRes* **2018**, *7*, 93–104.
[39] F. Blanc, in *Nanotechnol. Catal*, Wiley-VCH, Weinheim, **2017**, pp. 1003–1028.
[40] F. A. Perras, T. Kobayashi, M. Pruski, *eMagRes* **2018**, *7*, 35–50.
[41] A. G. M. Rankin, J. Trébosc, F. Pourpoint, J.-P. Amoureux, O. Lafon, *Solid State Nucl. Magn. Reson.* **2019**, *101*, 116–143.
[42] I. B. Moroz, M. Leskes, *Annu. Rev. Mater. Res.* **2022**, *52*, —25–55.
[43] N. J. Brownbill, R. S. Sprick, B. Bonillo, S. Pawsey, F. Aussenac, A. J. Fielding, A. I. Cooper, F. Blanc, *Macromolecules* **2018**, *51*, 3088–3096.
[44] F. Blanc, S. Y. Chong, T. O. McDonald, D. J. Adams, S. Pawsey, M. A. Caporini, A. I. Cooper, *J. Am. Chem. Soc.* **2013**, *135*, 15290–15293.
[45] S. Grätz, M. de Olivera Junior, T. Gutmann, L. Borchardt, *Phys. Chem. Chem. Phys.* **2020**, *22*, 23307–23314.
[46] A. Demessence, D. M. D'Alessandro, M. L. Foo, J. R. Long, *J. Am. Chem. Soc.* **2009**, *131*, 8784–8786.
[47] R. Dawson, A. Laybourn, Y. Z. Khimyak, D. J. Adams, A. I. Cooper, *Macromolecules* **2010**, *43*, 8524–8530.
[48] D. R. Miller, C. W. Macosko, *Macromolecules* **1976**, *9*, 206–211.
[49] P. J. Flory, in *Princ. Polym. Chem*, Cornell University Press, Ithaca, New York, **1953**, pp. 347–398.
[50] A. K. Rappé, C. J. Casewit, K. S. Colwell, W. A. Goddard, W. M. Skiff, *J. Am. Chem. Soc.* **1992**, *114*, 10024–10035.
[51] T. D. Bennett, A. K. Cheetham, *Acc. Chem. Res.* **2014**, *47*, 1555–1562.

[52] V. Petkov, R. G. Difrancesco, S. J. L. Billinge, M. Acharya, H. C. Foley, *Philos. Mag. B* **1999**, *79*, 1519–1530.
[53] K. W. Chapman, P. J. Chupas, C. J. Kepert, *J. Am. Chem. Soc.* **2005**, *127*, 11232–11233.
[54] M. I. Mohideen, P. K. Allan, K. W. Chapman, J. A. Hriljac, R. E. Morris, *Dalton Trans.* **2014**, *43*, 10438–10442.
[55] C. Koschnick, R. Stäglich, T. Scholz, M. W. Terban, A. von Mankowski, G. Savasci, F. Binder, A. Schökel, M. Etter, J. Nuss, R. Siegel, L. S. Germann, C. Ochsenfeld, R. E. Dinnebier, J. Senker, B. V. Lotsch, *Nat. Commun.* **2021**, *12*, 3099.
[56] C. Castillo-Blas, J. M. Moreno, I. Romero-Muñiz, A. E. Platero-Prats, *Nanoscale* **2020**, *12*, 15577–15587.
[57] I. Romero-Muñiz, A. Mavrandonakis, P. Albacete, A. Vega, V. Briois, F. Zamora, A. E. Platero-Prats, *Angew. Chem. Int. Ed.* **2020**, *59*, 13013–13020.
[58] Z. H. Syed, Z. Chen, K. B. Idrees, T. A. Goetjen, E. C. Wegener, X. Zhang, K. W. Chapman, D. M. Kaphan, M. Delferro, O. K. Farha, *Organometallics* **2020**, *39*, 1123–1133.
[59] Y. Benseghir, A. Lemarchand, M. Duguet, P. Mialane, M. Gomez-Mingot, C. Roch-Marchal, T. Pino, M.-H. Ha-Thi, M. Haouas, M. Fontecave, A. Dolbecq, C. Sassoye, C. Mellot-Draznieks, *J. Am. Chem. Soc.* **2020**, *142*, 9428–9438.
[60] N. Landaluce, M. Perfecto-Irigaray, J. Albo, G. Beobide, O. Castillo, A. Irabien, A. Luque, A. S. J. Méndez, A. E. Platero-Prats, S. Pérez-Yáñez, *Sci. Rep.* **2022**, *12*, 8505.
[61] T. Ito, J. Fraissard, in *Proc. 5th Int. Conf. Zeolites* (Ed.: L. V. C. Rees), Heyden, London, **1980**, pp. 510–515.
[62] T. Meersmann, E. Brunner, *Hyperpolarized Xenon-129 Magnetic Resonance*, Royal Society Of Chemistry, Cambridge, **2015**.
[63] D. Wisser, M. Hartmann, *Adv. Mater. Interfaces* **2021**, *8*, 2001266.
[64] K. Trepte, J. Schaber, S. Schwalbe, F. Drache, I. Senkovska, S. Kaskel, J. Kortus, E. Brunner, G. Seifert, *Phys. Chem. Chem. Phys.* **2017**, *19*, 10020–10027.
[65] F. Kolbe, S. Krause, V. Bon, I. Senkovska, S. Kaskel, E. Brunner, *Chem. Mater.* **2019**, *31*, 6193–6201.
[66] F. M. Wisser, K. Eckhardt, D. Wisser, W. Böhlmann, J. Grothe, E. Brunner, S. Kaskel, *Macromolecules* **2014**, *47*, 4210–4216.
[67] X. Kong, H. Deng, F. Yan, J. Kim, J. A. Swisher, B. Smit, O. M. Yaghi, J. A. Reimer, *Science* **2013**, *341*, 882–885.
[68] W. Yan, S. Li, T. Yang, Y. Xia, X. Zhang, C. Wang, Z. Yan, F. Deng, Q. Zhou, H. Deng, *J. Am. Chem. Soc.* **2020**, *142*, 16182–16187.
[69] Y. Fu, A. C. Forse, Z. Kang, M. J. Cliffe, W. Cao, J. Yin, L. Gao, Z. Pang, T. He, Q. Chen, Q. Wang, J. R. Long, J. A. Reimer, X. Kong, *Sci. Adv.* **2023**, *9*, eade6975.
[70] P. Berruyer, M. Lelli, M. P. Conley, D. L. Silverio, C. M. Widdifield, G. Siddiqi, D. Gajan, A. Lesage, C. Copéret, L. Emsley, *J. Am. Chem. Soc.* **2017**, *139*, 849–855.
[71] F. A. Perras, A. L. Paterson, Z. H. Syed, A. J. Kropf, D. M. Kaphan, M. Delferro, M. Pruski, *J. Phys. Chem. C* **2021**, *125*, 13433–13442.
[72] K. T. Mueller, *J. Magn. Reson. Ser. A* **1995**, *113*, 81–93.
[73] J. M. Goetz, J. Schaefer, *J. Magn. Reson.* **1997**, *127*, 147–154.
[74] M. Bertmer, H. Eckert, *Solid State Nucl. Magn. Reson.* **1999**, *15*, 139–152.

Manuscript received: July 28, 2023
Accepted manuscript online: August 30, 2023
Version of record online: September 26, 2023